Using 3D-printed fluidics to study the role of permeability heterogeneity on miscible density-driven convection in porous media

Ruichang Guo[1], Hanxing Sun[2], Hongsheng Wang[3], Yang Liu[2], Cheng Chen[1*]

[1] Department of Civil, Environmental and Ocean Engineering, Stevens Institute of Technology, Hoboken, NJ, USA

[2] Department of Mechanical Engineering, Virginia Tech, Blacksburg, VA, USA

[3] Bureau of Economic Geology, The University of Texas at Austin, Austin, TX, USA

Abstract: Miscible density-driven convection in porous media has important implications to the long-term security of geological carbon sequestration. Laboratory investigations of miscible density-driven convection in heterogeneous porous media have been greatly limited due to the challenge in constructing well-controlled heterogeneous permeability fields. In this study, three-dimensional (3D) printing was used to solve the challenge. Particularly, elementary sediment blocks were 3D printed to construct heterogeneous permeability fields having the desired mean, standard deviation, and spatial correlation length of permeability. A methanol-ethylene-glycol (MEG) solution was placed at the top of the permeability field to trigger miscible density-driven downward convection. Results showed that permeability heterogeneity caused noticeable uncertainty in the total MEG mass transferred into the permeability field, and the uncertainty increased with increasing correlation length of the permeability field. In a heterogeneous permeability field with a larger spatial correlation length, a larger effective vertical permeability

is in general favorable for solute mass transfer into the underlying porous medium. Conversely, in a heterogeneous permeability field with a shorter spatial correlation length, a larger effective vertical permeability does not necessarily lead to a higher mass transfer rate. This is because mass transfer across the top boundary through miscible density-driven convection depends on the flow recirculation near the interface. A large effective vertical permeability does not necessarily lead to fast flow recirculation because the former is measured in the vertical direction whereas the latter depends more on the internally-connected, high-permeability streaks within the domain. The 3D-printed elementary sediment blocks can be re-distributed to construct another permeability field easily, which greatly reduces the experimental time and thus significantly increases the total number of experiments that can be conducted, thereby approaching the ergodicity requirement when a large number of random permeability fields is needed.

Keywords: density-driven convection | porous media | permeability heterogeneity | 3D printing | geological carbon sequestration

* Corresponding author: Cheng Chen (cchen6@stevens.edu)

1. Introduction

Porous media are ubiquitous in natural and industrial processes, where complex fluid flow, mass transfer, and chemical reactions occur (Fredd and Fogler 1998, Gong and Gu 2015, Guo et al. 2020, Dudukovic et al. 2021, Kou et al. 2021, Qu et al. 2023). Miscible density-driven convection in porous media is a fundamental phenomenon of mass transfer, which has a wide range of applications in solute transport in groundwater aquifers (Simmons et al. 2001), saltwater intrusion in coastal aquifers (Kopsiaftis et al. 2009), and nuclear waste disposal (Neretnieks and Winberg-Wang 2019). Particularly, miscible density-driven convection in porous media has received increasing attention in the context of geological carbon sequestration (GCS), a promising solution to mitigating global climate change, because solubility trapping is one of the major trapping mechanisms for injected CO_2, which can be greatly enhanced by miscible density-driven convection (Xu et al. 2006, Chen and Zhang 2010, Farajzadeh et al. 2011, Chen et al. 2013).

Deep saline aquifers are considered promising geological formations for long-term CO_2 storage because of its vast storage capacity at the global scale. After injection into a deep saline aquifer, CO_2 migrates upwards due to buoyancy and accumulates beneath an impermeable cap rock. The accumulation of CO_2 under the cap rock poses a leaking risk. Dissolution of CO_2 into brine increases the brine density near the cap rock, which results in an unstable density stratification with the denser CO_2-rich brine solution sitting over the lighter, unaffected brine in the bottom of the aquifer. Under certain conditions, the unstable density stratification triggers miscible density-driven convection, which moves dissolved CO_2 away from the cap rock, thereby accelerating subsequent CO_2 dissolution across the CO_2-brine interface and mitigating the leaking risk at the cap rock (Chen et al. 2013). The enhanced CO_2 dissolution caused by miscible density-driven convection is referred to as convective dissolution or convective mixing, which is favorable for the long-term security of GCS (Yang and Gu 2006, Chen et al. 2013).

Miscible density-driven convection in porous media was first studied by Horton and Rogers (1945) and Lapwood (1948), which is commonly referred to as the Rayleigh-Darcy convection or Horton-Rogers-Lapwood convection. Rayleigh-Darcy convection in homogeneous porous media has been studied extensively (Ennis-King and Paterson 2005, Farajzadeh et al. 2007, Neufeld et al. 2010, Slim and Ramakrishnan 2010, Slim et al. 2013, Emami-Meybodi et al. 2015, Shi et al. 2018, Mahmoodpour et al. 2019, Tang et al. 2019). The Rayleigh number, Ra, is used to characterize the gravitational instability of the system. The critical Ra, the minimum Ra for triggering density-driven convection in a porous medium, can be determined by theoretical analysis (Slim and Ramakrishnan 2010), direct numerical simulation (Chen et al. 2013), and laboratory experiments(Guo et al. 2021). Other important system properties are the onset time of density-driven instability and mass transfer across the top boundary. The former refers to the time needed to trigger miscible density-driven convection, whereas the latter describes the amount of solute mass that migrates into the underlying porous media through the density-driven convection. These two properties are critical to evaluating the fate of injected CO_2 and total storage capacity in a GCS project. Numerous simulations and experiments have been developed to determine the onset time (Riaz et al. 2006, Farajzadeh et al. 2007, Pau et al. 2010, Liyanage et al. 2019) and mass transfer rate (Neufeld et al. 2010, Slim et al. 2013, Slim 2014, Newell et al. 2018, Mahmoodpour et al. 2019, Erfani et al. 2022).

The permeability distribution in a natural geological formation is in general highly heterogeneous. Convective dissolution of injected CO_2 in a heterogeneous formation is different from that in a homogeneous formation (Wang et al. 2021). Therefore, it is critical to develop fundamental understanding of the role of permeability heterogeneity on miscible density-driven convection in porous media. Due to the challenges in constructing well-controlled heterogeneous porous media in the laboratory, very limited experimental studies have been conducted. In these limited experimental studies, heterogeneous porous media were commonly layered or block-wise sand packs (Jose et al. 2004, Agartan et al. 2015, Taheri et al. 2018, Agartan et al. 2020, Bharath and Flynn 2021, Wang et al. 2021). As a consequence, Rayleigh-Darcy convection in heterogeneous porous media were studied primarily by direct numerical simulations (Farajzadeh et al. 2011, Cheng et al. 2012, Ranganathan et al. 2012, Chen et al. 2013, Kong and Saar 2013, Limare et al. 2019, Nield and Kuznetsov 2019, Gjengedal et al. 2020, Li et al. 2020, Li et al. 2020, Yang et al. 2021).

In this study, we developed a quasi-two-dimensional fluidic device based on the three-dimensional (3D) printing technology (Gjengedal et al. 2020, Almetwally and Jabbari 2021, Dudukovic et al. 2021) to solve the challenge in constructing well-controlled heterogeneous permeability fields. Particularly, elementary "digital sediment" blocks were 3D printed to construct a heterogeneous permeability field which had the desired mean, standard deviation, and spatial correlation length of permeability. We focused on the role of the spatial correlation length of a heterogeneous permeability field on miscible density-driven convection and the associated mass transfer into the porous medium.

2. Materials and Methodology

2.1. Generation of heterogeneous permeability fields

The permeability of geological formations usually follows a log-normal distribution (Chen et al. 2013, Loschko et al. 2018). The log permeability field is defined as

$$Y = \log(k), \quad (1)$$

where *k* is permeability. The mean and variance of the permeability field can be calculated using $\mu_k = e^{\mu_Y+\frac{\sigma_Y^2}{2}}$ and $\sigma_k^2 = \left(e^{\sigma_Y^2}-1\right)e^{2\mu_Y+\sigma_Y^2}$, where μ_Y and σ_Y are the mean and standard deviation of Y, respectively. In this study, we modeled the Y field using a Gaussian random field with a given covariance function (Chen et al. 2013, Guo et al. 2022). An exponential function is used as the covariance function (Rubin 2003), defined as:

$$c(\mathbf{s}) = \sigma_Y^2 exp\left[-\left(s_x^2/L_x^2 + s_y^2/L_y^2\right)^{1/2}\right], \tag{2}$$

where $\mathbf{s} = \left[s_x, s_y\right]^T$ is the separation vector between two points, and L_x and L_y are the spatial correlation lengths in the x and y directions, respectively. The log permeability field, **Y**, is written as $\mathbf{Y}=\left[Y_1, Y_2, Y_3, ..., Y_N\right]^T$, where N is the total block number. The covariance matrix, $\mathbf{C_Y}$, is defined as the expected value matrix of the product of **Y** and $\mathbf{Y}^T$, $\mathbf{C_Y} = E[\mathrm{YY}^T]$. $\mathbf{C_Y}$ is symmetric and positive definite and thus can be decomposed as $\mathbf{C_Y} = \mathbf{LL}^T$ using the Cholesky method, where **L** is a lower triangular matrix and $\mathbf{L}^T$ is an upper triangular matrix. Assuming that ξ is a vector of N uncorrelated normally distributed random numbers with zero mean and unit variance, **Y** can be generated as

$$\boldsymbol{Y} = \mu_Y \mathbf{I} + \mathbf{L}\xi, \tag{3}$$

where **I** is a vector of size N and all entries have a value of one (Chen and Zeng 2015).

2.2. Construction of heterogeneous permeability fields using 3D printing

Fig. 1a illustrates a realization of a heterogeneous permeability field, which was generated using a Gaussian random field as described in Section 2.1. The threshold method was used to convert the continuously distributed permeability field into a discrete, binary permeability field to allow for convenient construction of such a heterogeneous porous medium using 3D printing. In this work, a permeability field was discretized into 10 × 10 cells. The cells with permeability higher than the mean of the permeability field were constructed using 3D-printed porous blocks having grains with diameter of 3 mm. The other cells, which had permeability lower than the mean of the permeability field, were constructed using 3D-printed porous blocks having grains with diameter of 2 mm. The 3D printer deposited photocurable acrylic resin and wax layer by layer, which is ideal for printing 3D objects with fine features. The resin was transparent and used to fabricate the spherical particles, whereas the wax was used as the supporting material during the 3D printing process. In the post-processing stage, the wax was melted and removed from the pore spaces between spherical particles, which allowed the delicate features and complex internal cavities to be thoroughly cleaned without damage.

In this study, we used the discrete element method (Fan et al., 2019) to design two types of "digital sediment" blocks and then used 3D printing to fabricate them, as shown in Fig. 1b. These two types of sediment blocks were packed with uniform, full spherical particles having diameters of 2 mm and 3 mm, respectively. Both types of sediment blocks were 3D-printed with a spatial resolution of 13 μm and had overall dimensions of 2 cm × 2 cm × 2 cm. The one dimensional (1D) size of the sediment block (2 cm) was carefully selected to ensure that it was larger than the statistical representative elementary volume (sREV) (Zhang et al. 2000, Chen et al. 2008, Chen et al. 2009) size and in the meanwhile adequately small compared to the overall sand box so that a heterogeneous permeability field can be represented. To determine the sREV size for permeability in a particular sample, we fixed the subdomain size and moved it throughout the entire sample. At each subdomain location, we obtained the value of permeability. Therefore, at the end of the iteration, we obtained a larger number of permeability values, from which we calculated the mean and standard deviation. We then increased the subdomain diameter and repeated this process. Our recent study (Fan et al., 2018) showed that the sREV size for these spherical particles used to construct the 3D-printed sediment blocks was approximately four times of the average sediment grain diameter, when the sREV size was defined as the subdomain size at which the ratio of standard deviation of permeability to mean permeability was 10%. Therefore, from the permeability perspective, a sediment block having a 1D size of 2 cm is larger than the sREV size for the spherical particles having diameters of 2 mm and 3 mm. In addition, the size of 2 cm is small compared to the sand box so that 10 × 10 sediment blocks can be placed to represent the permeability heterogeneity.

Particularly, the gray area in Fig. 1b indicates the high-permeability region, which was constructed using the 3D-printed sediment blocks having 3 mm grain diameter, whereas the yellow area is the low-permeability region and was constructed using the sediment blocks having 2 mm grain diameter. Table 1 summarizes the laboratory-measured properties of these "digital sediment" blocks. The permeability values of these 3D-printed sediment blocks were measured in the laboratory. In the experiment, the sediment block was wrapped with a flexible rubber tube, which sealed the four lateral sides of the block, thereby forcing water to flow in the longitudinal flow direction . The permeability of the block was then calculated using the pressure difference and flow rate based on the Darcy's law.

Table 1. Properties of 3D-printed "digital sediment" blocks.

Grain diameter, *d* (mm)	Block dimensions	Permeability, *k* ($\times 10^{-12}$ m^2)	Porosity, ϕ (%)
2	2 cm × 2 cm × 2 cm	95.0	41.9
3	2 cm × 2 cm × 2 cm	526.4	44.2

2.3. Experimental setup

Fig. 1c demonstrates the fluidics experiment setup. The sand box was fabricated using transparent acrylic panels. The refraction index of acrylic panels is 1.49. The porous medium was constructed by stacking 10 × 10 3D-printed sediment blocks, leading to total dimensions of 20 cm × 20 cm × 2 cm (i.e., height × width × thickness). The transparent resin used to 3D print the spherical particles allowed direct observations of density-driven convection within the pore spaces. An analogous fluid was placed in the top fluid reservoir to trigger miscible density-driven downward convection that penetrated into the underlying 3D-printed porous medium. An impermeable panel was placed on the sediment blocks to eliminate the impact of fluid flow when the analogous fluid was injected into the top fluid reservoir. After the reservoir was filled, the impermeable panel was removed to trigger downward convection (Guo et al. 2021). In this work, a mixture of 40% mass fraction of methanol and 60% mass fraction of ethylene glycol formed the methanol ethylene glycol (MEG) fluid, which was then mixed with water to surrogate a CO_2-saturated brine solution. Fig. 1d illustrates the laboratory-measured MEG-water solution density as a function MEG mass concentration. The MEG solution density increased approximately linearly with the MEG mass concentration and reached the maximum when the MEG mass concentration was 50%. In addition, at a MEG mass concentration of 50%, the MEG solution density was higher than water by 11 kg/m^3, which is approximately equal to the density increase in a CO_2-saturated brine solution (Chen et al., 2013). This implies that the maximum increased gravitational acceleration due to the dissolved MEG, calculated as $\Delta\rho g/\rho_0$, is around 0.1 m/s^2, which is the same as that in a CO_2-saturated brine solution. Therefore, similar to a previous study(Guo et al. 2021), we used a MEG-water solution having a 50% MEG mass concentration in the top fluid reservoir. A blue dye was mixed in the solution as a tracer.

Ra is defined as $Ra = \Delta\rho g\bar{k}_v H/(\rho_0\phi\nu D)$, where $\Delta\rho$ is the density difference between the initial MEG-water solution and water (kg/m^3); g is gravitational acceleration (m/s^2); $\overline{k_v}$ is the effective vertical permeability of the entire porous medium (m^2), calculated from the overall flow rate and pressure gradient in the vertical direction obtained using a reservoir simulator; H is the characteristic length, which is the height of the entire porous medium (m); ρ_0 is the density of water (kg/m^3); ϕ is the average medium porosity; ν is the kinematic viscosity of water (m^2/s); D is the effective diffusivity of MEG in the porous medium (m^2/s).

Two spatial correlation lengths, 2 cm and 4 cm, were used to build the heterogeneous permeability fields separately. For each correlation length, eight realizations of the random permeability fields were generated to approach the ergodicity requirement. Therefore, we constructed in total 16 heterogeneous permeability fields and conducted the experiment for 16 times. Each of the permeability field realization was constructed using 50 sediment blocks having 2-mm particle diameter and 50 sediment blocks having 3-mm particle diameter, as described in Section 2.2.

Therefore, all of the 16 permeability field realizations had the same arithmetic average and standard deviation of permeability, which were 310.7×10^{-12} m^2 and 216.8×10^{-12} m^2, respectively.

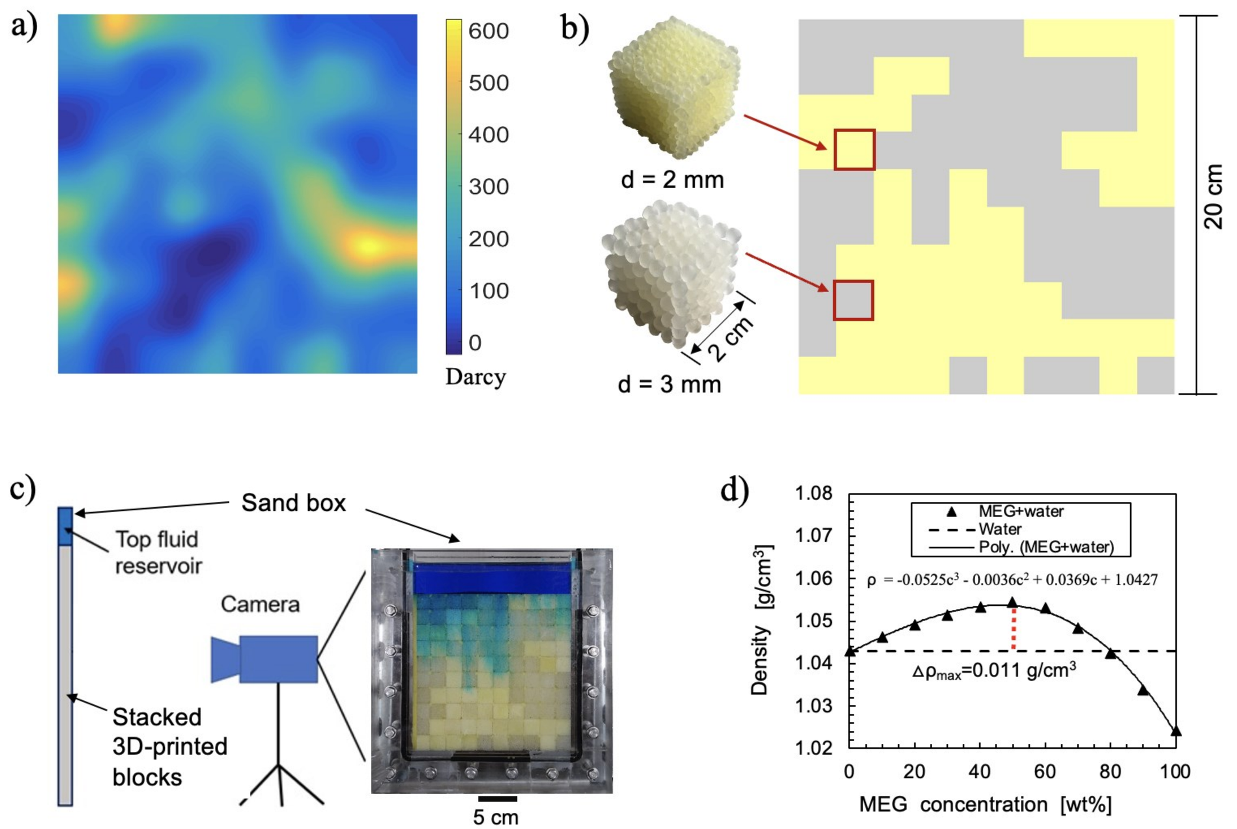

Fig. 1. a) A realization of a heterogeneous permeability field, b) a binary approximation of the heterogeneous permeability field constructed using 3D-printed sediment blocks having grain diameters of 2 mm and 3mm, c) laboratory experiment setup, and d) laboratory-measured density of MEG-water solution as a function of MEG mass concentration (triangular markers), with the solid line being the polynomial fitting curve.

2.4. Mass flux across the top boundary

The MEG mass transfer across the top boundary was calculated using digital image processing based on mass balance. During miscible density-driven convection, the penetration front movement was adequately slow. In addition, the local convective flow enhanced the dispersion coefficient for solute transport. These suggested that MEG was adequately mixed behind the penetration front, leading to homogeneous solute concentration behind the penetration front (Salehin et al. 2004, Chen and Zeng 2015). Therefore, the MEG concentration as a function of time can be calculated as:

$$C_m(t) = V_r C_{m,0} / (V_r + \sum(\phi_i A_i b)), \tag{4}$$

where V_r is the volume of top fluid reservoir, $C_{m,0}$ is the initial MEG mass concentration in the top fluid reservoir, ϕ_i is the porosity of the local sediment block, A_i is the area of the local sediment block, and b is the thickness of the porous medium. Particularly, A_i presents all porous medium area behind the penetration front (i.e., the porous medium region that the penetration front has swept), which were determined by tracking the penetration front boundary using digital imaging processing(Guo et al. 2021). The total MEG mass within the porous medium at time *t* can be calculated as: $M(t) = C_m(t) \sum(\phi_i A_i b)$. The MEG mass flux (kg/(m^{2}s)), defined as MEG mass transferred across a unit boundary area per unit time, is calculated as the total MEG mass increment in the porous medium over two consecutive measurement times normalized by the total top boundary area and the time increment.

2.5. Numerical simulation

In this study, numerical simulation was conducted to compare with the experimental observations. Particularly, we numerical solved the following governing equations (Ennis-King et al. 2005, Xu et al. 2006, Rapaka et al. 2008, Chen et al. 2013) (xxx) that describe miscible density-driven convection in porous media:

$$\mu \mathbf{k}^{-1} \boldsymbol{u} = -\nabla p + \rho g \boldsymbol{e}_y, \tag{5}$$

$$\nabla \cdot \boldsymbol{u} = 0 , \tag{6}$$

$$\phi \frac{\partial C_m}{\partial t} + \boldsymbol{u} \cdot \nabla C_m = \phi D \nabla^2 C_m, \tag{7}$$

$$\rho = \rho_0 (1 + \beta C_m) , \tag{8}$$

where μ is the dynamic viscosity, $\mathbf{k}$ is the permeability tensor of the heterogeneous porous media, p is the fluid pressure, ρ is the density of the water-MEG solution, $\boldsymbol{e}_y$ is the unit vector in the vertical direction, $\boldsymbol{u}$ is the Darcy velocity vector in the two-dimensional domain, C_m is the MEG mass concentration in the solution, ρ_0 is the water density, and β is the expansion coefficient which describes the relationship between dissolved MEG concentration and solution density. In the simulation, the Boussinesq approximation was adopted to assume that the dissolution of MEG in water affected only the density of water (Chen et al. 2013). The 16 heterogeneous permeability fields, as described in Section 2.3, were used in the numerical simulations. The computational domain was discretized into 200 $\times$ 200 cell blocks, the same boundary conditions as in the experiment were applied, and the implicit finite difference method (Chen 2016) was adopted to solved the coupled partial differential equations as shown in Equations 5-8.

3. Results and Discussion

3.1. Development of miscible density-driven convection

Fig. 2 illustrates the temporal evolutions of MEG downward penetration. The Ra numbers in the top and bottom experiments were 1934 and 2260, respectively. The onset of instability occurred in high-permeability regions (i.e., sediment blocks having 3-mm grain diameter). At the time scale of 1 min, MEG-rich fingers had developed to a noticeable extent, and after that the fingers developed preferentially following the high-permeability regions. Previous studies showed that three mechanisms control convective mixing in a heterogeneous permeability field, which are dispersion, channeling, and fingering (Farajzadeh et al. 2011, Ranganathan et al. 2012, Chen et al. 2013). Fingering occurs when the permeability's standard deviation is low. Channeling occurs when the permeability's standard deviation is moderate to high, associated with a moderate to large spatial correlation length. In contrast, dispersion occurs when the permeability's standard deviation is moderate to high, associated with a small spatial correlation length. The density-driven downward convection in this study was controlled primarily by channeling due to the combination of heterogeneity and spatial correlation length in the permeability fields. Particularly, at later times (i.e.,5 min and 10 min) MEG-rich fingers developed preferentially following the high-permeability blocks in both experiments, whereas the low-permeability blocks acted as barriers which hindered the downward penetration of the MEG-rich fingers. In addition, preferential transport of MEG-rich solution along the vertical contact edges between sediment blocks was observed. Although mechanical stress was applied on the sand box panels to compress the sediment blocks to minimize preferential flows, improved methods for sediment block concatenation are needed in future studies to entirely eliminate preferential flows.

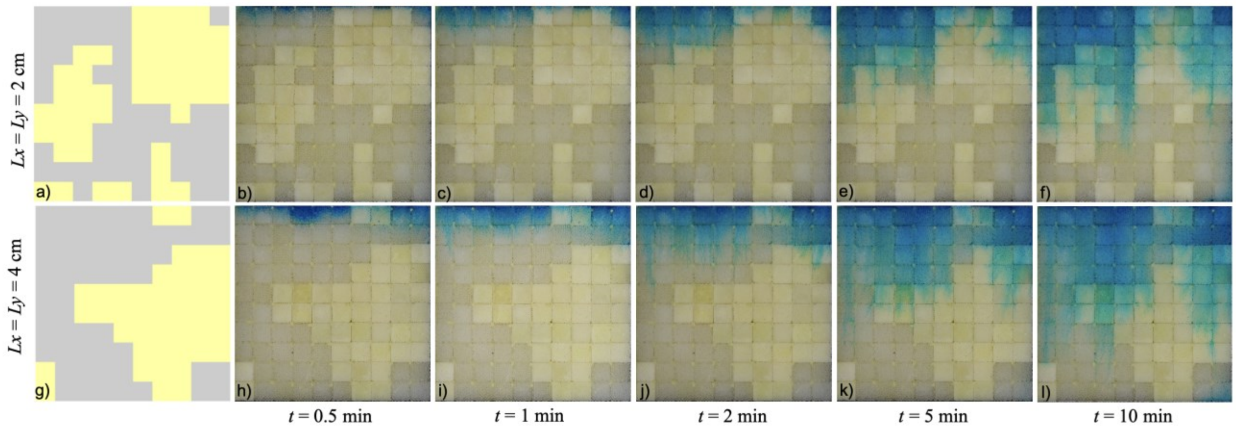

Fig. 2. Development of density-driven convection in heterogeneous permeability fields having the same mean and standard deviation of permeability. The top and bottom permeability fields had spatial correlation lengths of 2 cm and 4 cm, respectively. The gray and yellow regions were constructed using 3D-printed sediment blocks with grain diameters of 3 mm and 2 mm, respectively.

3.2. Mass flux across the top boundary

Fig. 3 illustrates the development of the penetration fronts, as well as MEG mass flux and total transferred MEG mass across the top boundary as a function of time. The MEG-rich solution front preferentially developed along the high-permeability 3D-printed sediment blocks. The development of miscible density-driven convection can be characterized into the diffusive regime, velocity-growth regime, flux-growth regime, quasi-steady regime, and shutdown regime (Mahmoodpour et al. 2019). The mass transfer is dominated primarily by molecular diffusion in the diffusive and velocity-growth regimes. The mass flux across the top boundary continuously decays at early times because the MEG mass transferred into the underlying porous medium diminishes the concentration gradient across the penetration front. At a later time, the mass flux contributed by convection starts to dominate over that contributed by molecular diffusion. At this point, the total mass flux starts to increase, which marks the beginning of the flux-growth regime. Fig. 3 illustrates that the onset of the flux-growth regime occurred approximately after eight minutes in both experiments.

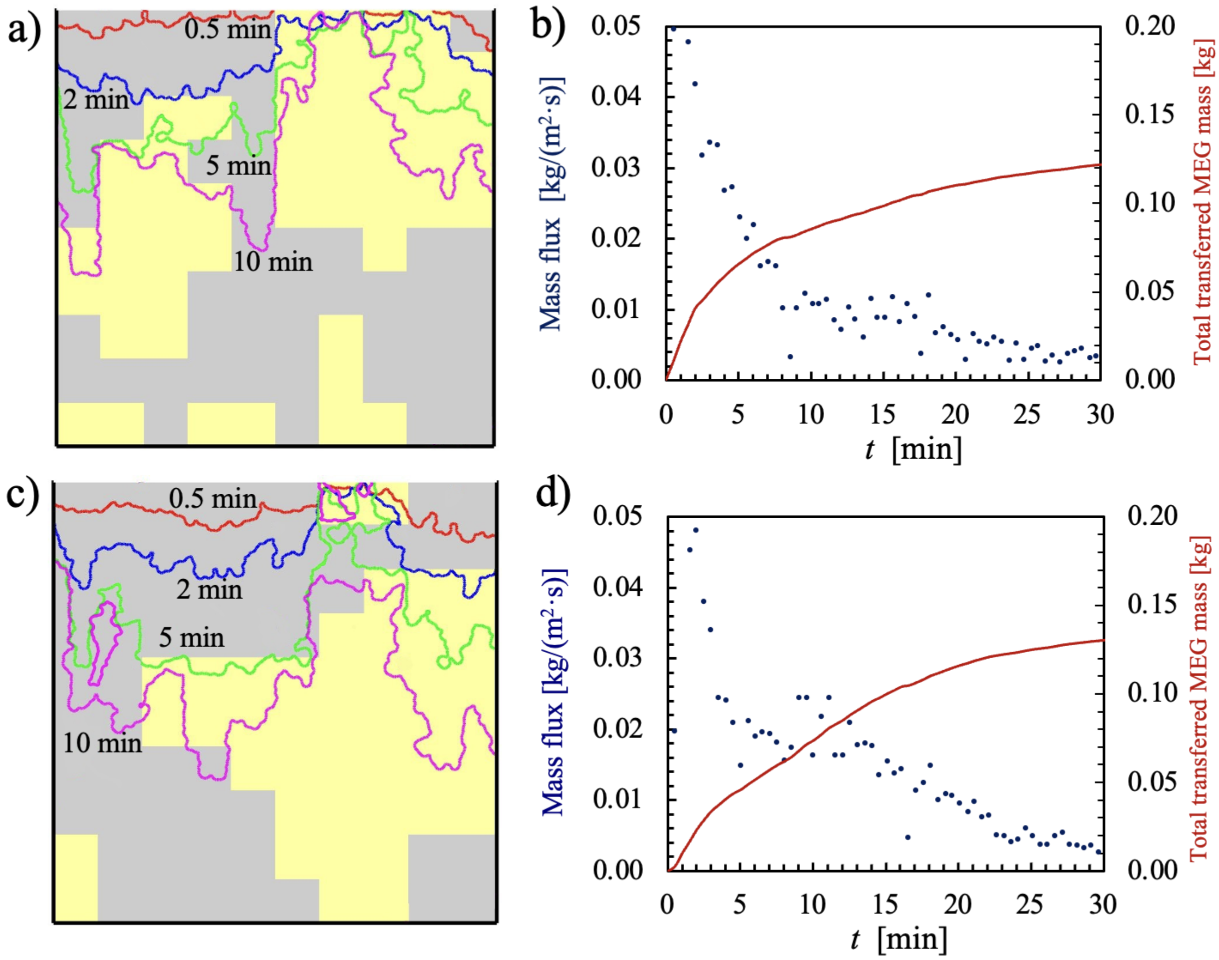

Fig. 3. a) Density-driven penetration fronts at 0.5 min, 2 min, 5 min, and 10 min, and b) mass flux and total transferred mass of MEG across the top boundary as a function of time in a heterogeneous permeability field having a spatial correlation length of 2 cm. c) Density-driven penetration fronts

at 0.5 min, 2 min, 5 min, and 10 min, and d) mass flux and total transferred mass of MEG across the top boundary as a function of time in a heterogeneous permeability field having a spatial correlation length of 4 cm. The gray and yellow regions were constructed using 3D-printed sediment blocks with grain diameters of 3 mm and 2 mm, respectively.

3.3. Uncertainty in mass flux

Fig. 3 demonstrates only one realization of the heterogeneous permeability field for each spatial correlation length. As described previously, in order to approach the ergodicity requirement, eight realizations of the random permeability field for each correlation length were constructed; we then conducted the miscible density-driven convection experiment on each of the realization. **Fig. 4a** and Fig. 4b illustrate the total MEG mass transfer amounts against time measured in these experiments, as well as the means and standard deviations. The result showed that the average MEG mass transfer rate was similar for both spatial correlation lengths. In other words, the average total transferred MEG mass across the top boundary at the same experimental time was similar in both scenarios. However, for the correlation length of 4 cm, the collective behavior of the measured mass-time curves showed a more scattered pattern, leading to a wider envelope. This indicates that a larger spatial correlation length in a heterogeneous permeability field causes a higher uncertainty in the mass transfer. Figures 4c and 4d illustrate the corresponding numerical simulations of the experimental processes demonstrated in Figures 4a and 4b. The simulations showed the same observation that a larger spatial correlation length caused higher uncertainty in the total transferred mass, leading to a wider envelope. The comparison also showed that at early times (i.e., , less than 6 min) the average total transferred mass in the experiment was slightly higher than that in the simulation, which may be caused by initial disturbance in the experiment that was not accounted for in the numerical simulation. The difference between experimentally-measured and numerically-simulated total dissolved MEG mass was measured by the root mean square error (RMSE), which is calculated as $RMSE = \sqrt{\sum_{i=1}^{N_m} \left\| M_i^{experiment} - M_i^{simulation} \right\|^2 / N_m}$, where N_m is the total number of experimental data points. The RMSEs were 0.00799 kg and 0.00719 kg for the heterogeneous permeability fields having a spatial correlation length of 2 cm and 4 cm, respectively.

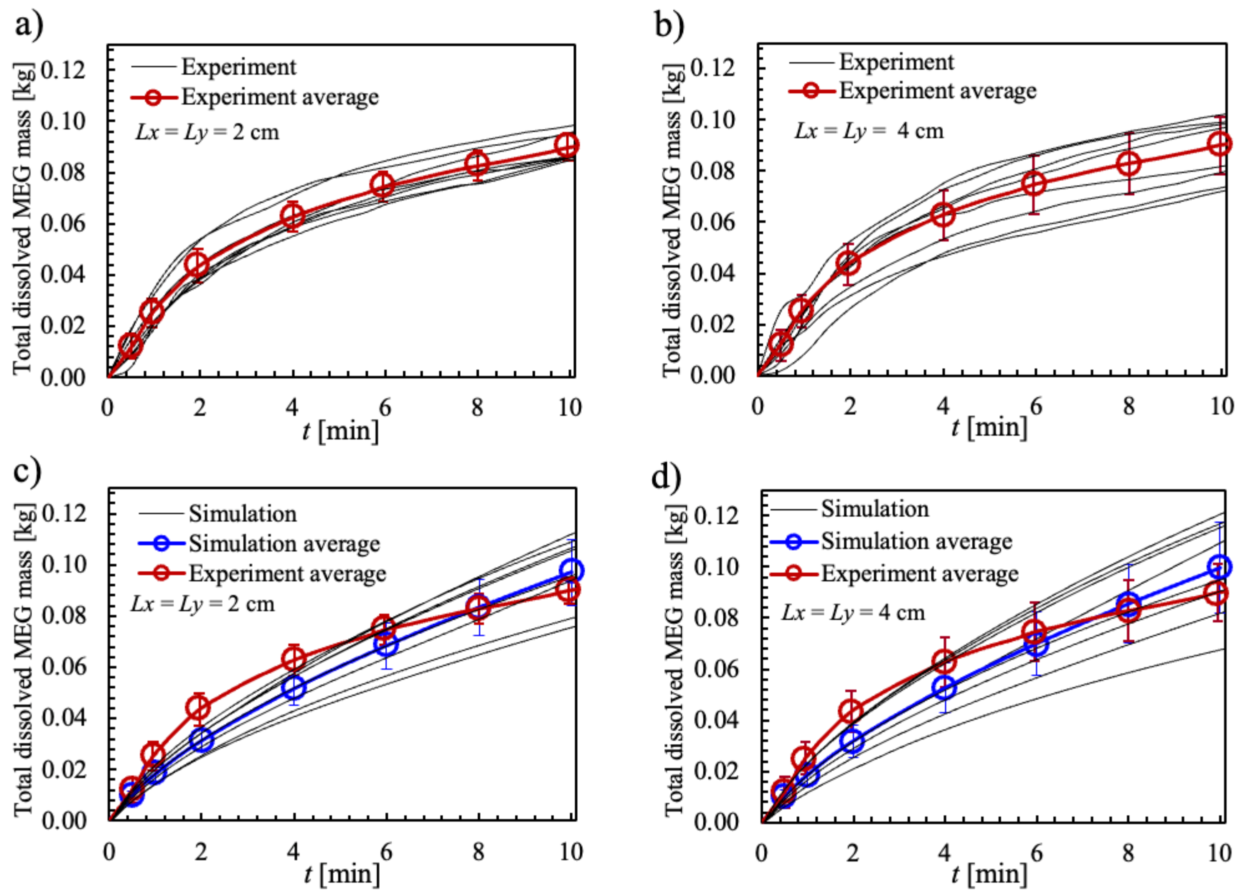

Fig. 4. Total transferred MEG mass as a function of time across the top boundary of a heterogeneous permeability field having a spatial correlation length of a) 2 cm, and b) 4 cm. Each black curve is the experimental measurement obtained from a specific realization of heterogeneous permeability field. The red solid curve and error bar indicate the average and standard deviation, respectively. Corresponding numerical simulation of the total transferred MEG mass as a function of time in the heterogeneous permeability fields having a spatial correlation length of c) 2 cm, and d) 4 cm. The blue solid curve and error bar indicate the average and standard deviation of the simulation results, respectively. For comparison, the average and standard deviation of the experimental results are also shown in Figures c and d.

Fig. 5 demonstrates the relation between total transferred MEG mass and the effective vertical permeability of the heterogeneous permeability field, $\bar{k}_v$, in the 16 permeability field realizations. First, it was observed that $\bar{k}_v$ was always lower than the arithmetic average of the permeability field (i.e., 310.7×10^{-12} m^2), which was caused by the spatial heterogeneity in the permeability field. Second, no noticeable correlation between the total transferred MEG mass and $\bar{k}_v$ was observed in porous media with a spatial correlation length of 2 cm (i.e., Fig. 5a), whereas an overall positive correlation was observed in porous media with a spatial correlation length of 4 cm (i.e., Fig. 5b). This was because MEG mass transfer across the top boundary depended on the downward convective flow near the interface, which caused nearby upward fluid flow because of mass balance (Chen and Zhang 2010). The downward and upward flows led to flow recirculation near the top boundary of the porous medium, which regulated mass transfer across the interface. A large effective vertical permeability does not necessarily lead to fast flow recirculation because the former is measured in the vertical direction whereas the latter depends more on the internally-connected, high-permeability streaks. Therefore, the spatial correlation length of the permeability field plays a critical role on flow recirculation. In the porous medium with a spatial correlation length of 4 cm, when the effective vertical permeability was high, it was relatively easier to find spatially-connected high-permeability streaks, which facilitated the development of flow recirculation near the top boundary; when the effective vertical permeability was low, it was likely to find spatially-connected low-permeability barriers that hampered the development of flow recirculation. Conversely, the spatial correlation length of 2 cm led to isolated and spotted permeability structure, which diminished the relationship between effective vertical permeability and internal flow recirculation. This finding suggests that in a heterogeneous permeability field with a shorter spatial correlation length, a larger effective vertical permeability does not necessarily lead to a larger amount of solute mass transfer into the underlying porous medium by means of density-driven convection. In comparison, in a heterogeneous permeability field with a larger spatial correlation length, a larger effective vertical permeability is in general favorable for mass transfer into the underlying porous medium.

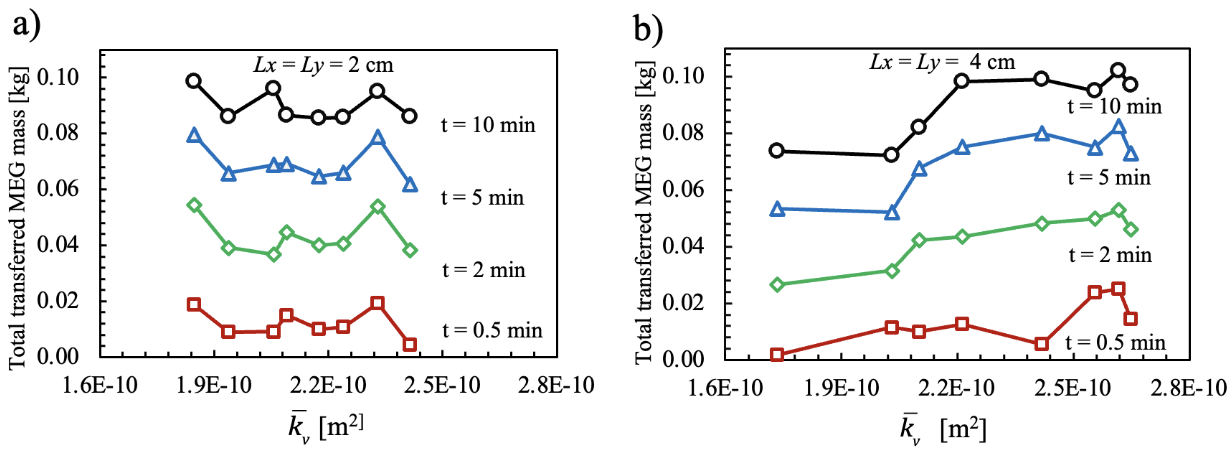

Fig. 5. Total transferred MEG mass as a function the effective vertical permeability of a heterogeneous permeability field having a spatial correlation length of a) 2 cm, and b) 4 cm, respectively.

4. Conclusion and Implications

We developed a 3D-printing-based fluidic device to study the role of permeability heterogeneity on miscible density-driven convection in porous media. Experimental results showed that permeability heterogeneity caused noticeable uncertainty in the total transferred MEG mass, and the uncertainty increased with increasing spatial correlation length of the permeability field. In a heterogeneous permeability field with a larger spatial correlation length, a larger effective vertical permeability is in general favorable for solute mass transfer into the underlying porous medium. Conversely, in a heterogeneous permeability field with a shorter spatial correlation length, a larger effective vertical permeability does not necessarily lead to a larger amount of solute mass transfer. This is because mass transfer across the top boundary through miscible density-driven convection depends on the local flow recirculation near the interface. A large effective vertical permeability does not necessarily lead to fast flow recirculation because the former is measured in the vertical direction whereas the latter depends more on the internally-connected, high-permeability streaks within the domain. Therefore, the spatial correlation length of the permeability field plays a critical role on flow recirculation. These research findings show that permeability heterogeneity not only refers to the spatial variation of permeability, but should also account for its spatial correlation length.

The 3D fluidics technology developed in this study makes it possible to construct known and well-controlled heterogeneous permeability fields in an efficient way, which solves the challenge in constructing heterogeneous porous media in the laboratory. Particularly, the 3D-printed elementary sediment blocks can be re-distributed to construct another permeability field easily, which greatly reduces the experimental time and thus significantly increases the total number of experiments that can be conducted, thereby approaching the ergodicity requirement when a large number of random permeability fields is needed. Although this study is focused on density-driven downward convection, the developed 3D printing technology and the research findings from this work have important applications to other subsurface flow and transport processes where the permeability heterogeneity is critical.

Acknowledgement

The authors are thankful to the financial support provided by the U.S. National Science Foundation's Division of Earth Sciences under the award number of EAR-2154295. Data is available through: https://doi.org/10.5281/zenodo.6416110.

Nomenclature

A_i	Area of porous medium corresponding to porous block i
b	Reservoir thickness
c	Covariance function
C_m	Mass concentration of MEG in water
$C_{m,0}$	Initial MEG mass concentration in the top fluid reservoir
$\mathbf{C}_\mathbf{Y}$	Covariance matrix
D	Effective diffusivity of MEG in the porous medium
d	Diameter
$\mathbf{e}_y$	Unit vector in the vertical direction
g	Gravitational acceleration
H	Characteristic length
$\mathbf{I}$	Identity matrix
k	Permeability
$\mathbf{k}$	Permeability tensor
$\bar{k}_v$	Effective vertical permeability of the entire porous medium
$\mathbf{L}$	Lower triangular matrix
L_x	Spatial correlation length in the x direction
L_y	Spatial correlation length in the y direction
M	MEG mass
N	Block number
N_m	Number of experimental measurements of total dissolved MEG
p	Fluid pressure
$\mathbf{s}$	Separation vector between two points

s_x	Separation distance in the *x* direction
s_y	Separation distance in the *y* direction
$\boldsymbol{u}$	Velocity vector
t	Time
V_r	Volume of fluid reservoir
x	Direction
β	Expansion coefficient
Y	Permeability field
y	Direction
μ_k	Mean of *k*
μ_Y	Mean of *Y*
ν	Kinematic viscosity of water
ξ	Vector with zero mean and unit variance
ρ	Density of water-MEG solution
ρ_0	Density of water
$\Delta\rho$	Density difference between the initial MEG-water solution and water
σ_k	Standard deviation of *k*
σ_Y	Standard deviation of *Y*
ϕ	Porosity of porous media

Reference

Agartan, E., T. H. Illangasekare, J. Vargas-Johnson, A. Cihan and J. Birkholzer (2020). "Experimental investigation of assessment of the contribution of heterogeneous semi-confining shale layers on mixing and trapping of dissolved CO2 in deep geologic formations." International Journal of Greenhouse Gas Control **93**.

Agartan, E., L. Trevisan, A. Cihan, J. Birkholzer, Q. L. Zhou and T. H. Illangasekare (2015). "Experimental study on effects of geologic heterogeneity in enhancing dissolution trapping of supercritical CO2." Water Resources Research **51**(3): 1635-1648.

Almetwally, A. G. and H. Jabbari (2021). "3D-Printing Replication of Porous Media for Lab-Scale Characterization Research." Acs Omega **6**(4): 2655-2664.

Bharath, K. S. and M. R. Flynn (2021). "Buoyant convection in heterogeneous porous media with an inclined permeability jump: an experimental investigation of filling box-type flows." Journal of Fluid Mechanics **924**.

Chen, C. (2016). "Multiscale imaging, modeling, and principal component analysis of gas transport in shale reservoirs." Fuel **182**: 761-770.

Chen, C., A. I. Packman and J. F. Gaillard (2008). "Pore-scale analysis of permeability reduction resulting from colloid deposition." Geophysical Research Letters **35**(7).

Chen, C., A. I. Packman and J. F. Gaillard (2009). "Using X-ray micro-tomography and pore-scale modeling to quantify sediment mixing and fluid flow in a developing streambed." Geophysical Research Letters **36**.

Chen, C. and L. Z. Zeng (2015). "Using the level set method to study the effects of heterogeneity and anisotropy on hyporheic exchange." Water Resources Research **51**(5): 3617-3634.

Chen, C., L. Z. Zeng and L. S. Shi (2013). "Continuum-scale convective mixing in geological CO2 sequestration in anisotropic and heterogeneous saline aquifers." Advances in Water Resources **53**: 175-187.

Chen, C. and D. X. Zhang (2010). "Pore-scale simulation of density-driven convection in fractured porous media during geological CO2 sequestration." Water Resources Research **46**.

Cheng, P., M. Bestehorn and A. Firoozabadi (2012). "Effect of permeability anisotropy on buoyancy-driven flow for CO2 sequestration in saline aquifers." Water Resources Research **48**.

Dudukovic, N. A., E. J. Fong, H. B. Gemeda, J. R. DeOtte, M. R. Ceron, B. D. Moran, J. T. Davis, S. E. Baker and E. B. Duoss (2021). "Cellular fluidics." Nature **595**(7865): 58-65.

Emami-Meybodi, H., H. Hassanzadeh, C. P. Green and J. Ennis-King (2015). "Convective dissolution of CO2 in saline aquifers: Progress in modeling and experiments." International Journal of Greenhouse Gas Control **40**: 238-266.

Ennis-King, J. and L. Paterson (2005). "Role of convective mixing in the long-term storage of carbon dioxide in deep saline formations." Spe Journal **10**(3): 349-356.

Ennis-King, J., I. Preston and L. Paterson (2005). "Onset of convection in anisotropic porous media subject to a rapid change in boundary conditions." Physics of Fluids **17**(8).

Erfani, H., M. Babaei, C. F. Berg and V. Niasar (2022). "Scaling CO2 convection in confined aquifers: Effects of dispersion, permeability anisotropy and geochemistry." Advances in Water Resources **164**.

Farajzadeh, R., P. Ranganathan, P. L. J. Zitha and J. Bruining (2011). "The effect of heterogeneity on the character of density-driven natural convection of CO2 overlying a brine layer." Advances in Water Resources **34**(3): 327-339.

Farajzadeh, R., H. Salimi, P. L. J. Zitha and H. Bruining (2007). "Numerical simulation of density-driven natural convection in porous media with application for CO2 injection projects." International Journal of Heat and Mass Transfer **50**(25-26): 5054-5064.

Fredd, C. N. and H. S. Fogler (1998). "Influence of transport and reaction on wormhole formation in porous media." Aiche Journal **44**(9): 1933-1949.

Gjengedal, S., V. Brotan, O. T. Buset, E. Larsen, O. A. Berg, O. Torsaeter, R. K. Ramstad, B. O. Hilmo and B. S. Frengstad (2020). "Fluid flow through 3D-printed particle beds: a new technique for understanding, validating, and improving predictability of permeability from empirical equations." Transport in Porous Media **134**(1): 1-40.

Gong, Y. B. and Y. A. Gu (2015). "Experimental Study of Water and CO2 Flooding in the Tight Main Pay Zone and Vuggy Residual Oil Zone of a Carbonate Reservoir." Energy & Fuels **29**(10): 6213-6223.

Guo, R. C., L. Dalton, D. Crandall, J. McClure, H. S. Wang, Z. Li and C. Chen (2022). "Role of heterogeneous surface wettability on dynamic immiscible displacement, capillary pressure, and relative permeability in a CO2-water-rock system." Advances in Water Resources **165**.

Guo, R. C., L. E. Dalton, M. Fan, J. McClure, L. Z. Zeng, D. Crandall and C. Chen (2020). "The role of the spatial heterogeneity and correlation length of surface wettability on two-phase flow in a CO2-water-rock system." Advances in Water Resources **146**.

Guo, R. C., H. X. Sun, Q. Q. Zhao, Z. H. Li, Y. Liu and C. Chen (2021). "A Novel Experimental Study on Density-Driven Instability and Convective Dissolution in Porous Media." Geophysical Research Letters **48**(23).

Horton, C. W. and F. T. Rogers (1945). "Convection Currents in a Porous Medium." Journal of Applied Physics **16**(6): 367-370.

Jose, S. C., M. A. Rahman and O. A. Cirpka (2004). "Large-scale sandbox experiment on longitudinal effective dispersion in heterogeneous porous media." Water Resources Research **40**(12).

Kong, X. Z. and M. O. Saar (2013). "Numerical study of the effects of permeability heterogeneity on density-driven convective mixing during CO2 dissolution storage." International Journal of Greenhouse Gas Control **19**: 160-173.

Kopsiaftis, G., A. Mantoglou and P. Giannoulopoulos (2009). "Variable density coastal aquifer models with application to an aquifer on Thira Island." Desalination **237**(1-3): 65-80.

Kou, Z. H., H. Wang, V. Alvarado, J. F. McLaughlin and S. A. Quillinan (2021). "Impact of sub-core scale heterogeneity on CO2/brine multiphase flow for geological carbon storage in the upper Minnelusa sandstones." Journal of Hydrology **599**.

Lapwood, E. R. (1948). "Convection of a Fluid in a Porous Medium." Proceedings of the Cambridge Philosophical Society **44**(4): 508-521.

Li, Q., W. H. Cai, B. X. Li and C. Y. Chen (2020). "Numerical Study of Density-Driven Convection in Laminated Heterogeneous Porous Media." Journal of Mechanics **36**(5): 665-673.

Li, Q., W. H. Cai, X. J. Tang, Y. C. Chen, B. X. Li and C. Y. Chen (2020). "The impact of heterogeneous anisotropy of porous media on density-driven convection." International Journal of Numerical Methods for Heat & Fluid Flow **30**(2): 956-976.

Limare, A., C. Jaupart, E. Kaminski, L. Fourel and C. G. Farnetani (2019). "Convection in an internally heated stratified heterogeneous reservoir." Journal of Fluid Mechanics **870**: 67-105.

Liyanage, R., J. J. Cen, S. Krevor, J. P. Crawshaw and R. Pini (2019). "Multidimensional Observations of Dissolution-Driven Convection in Simple Porous Media Using X-ray CT Scanning." Transport in Porous Media **126**(2): 355-378.

Loschko, M., T. Wohling, D. L. Rudolph and O. A. Cirpka (2018). "Accounting for the Decreasing Reaction Potential of Heterogeneous Aquifers in a Stochastic Framework of Aquifer-Scale Reactive Transport." Water Resources Research **54**(1): 442-463.

Mahmoodpour, S., B. Rostami, M. R. Soltanian and M. A. Amooie (2019). "Convective Dissolution of Carbon Dioxide in Deep Saline Aquifers: Insights from Engineering a High-Pressure Porous Visual Cell." Physical Review Applied **12**(3).

Neretnieks, I. and H. Winberg-Wang (2019). "Density-Driven Mass Transfer in Repositories for Nuclear Waste." Nuclear Technology **205**(6): 819-829.

Neufeld, J. A., M. A. Hesse, A. Riaz, M. A. Hallworth, H. A. Tchelepi and H. E. Huppert (2010). "Convective dissolution of carbon dioxide in saline aquifers." Geophysical Research Letters **37**.

Newell, D. L., J. W. Carey, S. N. Backhaus and P. Lichtner (2018). "Experimental study of gravitational mixing of supercritical CO2." International Journal of Greenhouse Gas Control **71**: 62-73.

Nield, D. A. and A. V. Kuznetsov (2019). "The Onset of Convection in an Anisotropic Heterogeneous Porous Medium: A New Hydrodynamic Boundary Condition." Transport in Porous Media **127**(3): 549-558.

Pau, G. S. H., J. B. Bell, K. Pruess, A. S. Almgren, M. J. Lijewski and K. N. Zhang (2010). "High-resolution simulation and characterization of density-driven flow in CO2 storage in saline aquifers." Advances in Water Resources **33**(4): 443-455.

Qu, H., Y. S. Hu, R. C. Guo, C. C. Lin, J. N. Xu, H. Jun and X. J. Chen (2023). "Experimental study on pore structure alteration of deep shale under liquid nitrogen freezing based on nuclear magnetic resonance." International Journal of Hydrogen Energy **48**(1): 51-66.

Ranganathan, P., R. Farajzadeh, H. Bruining and P. L. J. Zitha (2012). "Numerical Simulation of Natural Convection in Heterogeneous Porous media for CO2 Geological Storage." Transport in Porous Media **95**(1): 25-54.

Rapaka, S., S. Y. Chen, R. J. Pawar, P. H. Stauffer and D. X. Zhang (2008). "Non-modal growth of perturbations in density-driven convection in porous media." Journal of Fluid Mechanics **609**: 285-303.

Riaz, A., M. Hesse, H. A. Tchelepi and F. M. Orr (2006). "Onset of convection in a gravitationally unstable diffusive boundary layer in porous media." Journal of Fluid Mechanics **548**: 87-111.

Rubin, Y. (2003). "Applied Stochastic Hydrogeology." Oxford Univ. Press, N. Y.

Salehin, M., A. I. Packman and M. Paradis (2004). "Hyporheic exchange with heterogeneous streambeds: Laboratory experiments and modeling." Water Resources Research **40**(11).

Shi, Z., B. Wen, M. A. Hesse, T. T. Tsotsis and K. Jessen (2018). "Measurement and modeling of CO2 mass transfer in brine at reservoir conditions." Advances in Water Resources **113**: 100-111.

Simmons, C. T., T. R. Fenstemaker and J. M. Sharp (2001). "Variable-density groundwater flow and solute transport in heterogeneous porous media: approaches, resolutions and future challenges." Journal of Contaminant Hydrology **52**(1-4): 245-275.

Slim, A. C. (2014). "Solutal-convection regimes in a two-dimensional porous medium." Journal of Fluid Mechanics **741**: 461-491.

Slim, A. C., M. M. Bandi, J. C. Miller and L. Mahadevan (2013). "Dissolution-driven convection in a Hele-Shaw cell." Physics of Fluids **25**(2).

Slim, A. C. and T. S. Ramakrishnan (2010). "Onset and cessation of time-dependent, dissolution-driven convection in porous media." Physics of Fluids **22**(12).

Taheri, A., O. Torsaeter, E. Lindeberg, N. J. Hadia and D. Wessel-Berg (2018). "Qualitative and quantitative experimental study of convective mixing process during storage of CO2 in heterogeneous saline aquifers." International Journal of Greenhouse Gas Control **71**: 212-226.

Tang, Y. Q., Z. H. Li, R. Wang, M. L. Cui, X. Wang, Z. M. Lun and Y. Lu (2019). "Experimental Study on the Density-Driven Carbon Dioxide Convective Diffusion in Formation Water at Reservoir Conditions." Acs Omega **4**(6): 11082-11092.

Wang, S. J., Z. C. Cheng, Y. Zhang, L. L. Jiang, Y. Liu and Y. C. Song (2021). "Unstable Density-Driven Convection of CO2 in Homogeneous and Heterogeneous Porous Media With Implications for Deep Saline Aquifers." Water Resources Research **57**(3).

Xu, X. F., S. Y. Chen and D. X. Zhang (2006). "Convective stability analysis of the long-term storage of carbon dioxide in deep saline aquifers." Advances in Water Resources **29**(3): 397-407.

Yang, C. D. and Y. G. Gu (2006). "Accelerated mass transfer of CO2 in reservoir brine due to density-driven natural convection at high pressures and elevated temperatures." Industrial & Engineering Chemistry Research **45**(8): 2430-2436.

Yang, X. J., Q. Shao, H. Hoteit, J. Carrera, A. Younes and M. Fahs (2021). "Three-dimensional natural convection, entropy generation and mixing in heterogeneous porous medium." Advances in Water Resources **155**.

Zhang, D. X., R. Y. Zhang, S. Y. Chen and V. E. Soll (2000). "Pore scale study of flow in porous media: Scale dependency, REV, and statistical REV." Geophysical Research Letters **27**(8): 1195-1198.